

## Full paper

## High efficiency sandwich structure luminescent solar concentrators based on colloidal quantum dots

Guiju Liu<sup>a</sup>, Raffaello Mazzaro<sup>b</sup>, Yiqian Wang<sup>a,\*\*\*</sup>, Haiguang Zhao<sup>a,\*\*</sup>, Alberto Vomiero<sup>b,c,\*</sup><sup>a</sup> College of Physics & the State Key Laboratory, Qingdao University, No. 308 Ningxia Road, Qingdao, 266071, PR China<sup>b</sup> Division of Material Science, Department of Engineering Sciences and Mathematics, Luleå University of Technology, 971 87, Luleå, Sweden<sup>c</sup> Department of Molecular Sciences and Nanosystems, Ca' Foscari University of Venice, Via Torino 155, 30172, Venezia Mestre, Italy

## ARTICLE INFO

## Keywords:

Luminescent solar concentrators  
Sandwich structure  
CdSe/CdS QDs  
Microstructure  
External optical efficiency

## ABSTRACT

Luminescent solar concentrators (LSCs) have received significant attention because of their low cost, large-area and high efficiency sunlight energy harvesting. Colloidal core/shell quantum dots (QDs) are promising candidates as absorbers/emitters in LSCs. However, due to the limitation of QDs properties and device architectures, LSCs fabricated using QDs still face the challenges of low optical efficiency and limited long-term stability for the large-area LSCs. In this work, we synthesized CdSe/CdS QDs, and found that higher CdS shell growth temperature results in improved uniformity in structure and morphology and more suitable optical properties. Based on the CdSe/CdS QDs, a large-area ( $\sim 100\text{ cm}^2$ ) sandwich structure luminescent solar concentrator (LSC) was fabricated. By laminating the QDs layer between two sheets of optical clear glass, the reabsorption losses of the device can be reduced due to the decrease of photon escape. The as-fabricated sandwich structure device exhibits an external optical efficiency of  $\sim 2.95\%$  under natural sunlight illumination, which represents a 78% enhancement in efficiency over the single layer film LSCs based on CdSe/CdS QDs. More importantly, the sandwich structure can protect the QDs interlayer from the impact of the ambient environment (e.g. oxygen, moisture and alkalinity) and enhance the long-term stability of LSCs. Our work shows that the use of suitably tuned core-shell QDs and the sandwich structure in LSC architecture can dramatically enhance the external optical efficiency of LSC devices based on CdSe/CdS QDs.

## 1. Introduction

Today, the efficient conversion of solar energy to electrical/chemical energy has received an intensive worldwide attention due to the concerns of environmental sustainability and global warming [1–3]. Current commercial silicon solar cells have achieved a high power conversion efficiency (PCE) ( $> 20\%$ ) and long-term stability (lifetime  $> 25$  years with 90% of its initial efficiency) [4]. However, the cost of silicon photovoltaic (PV) modules is still quite high, which limits their further application [5]. To reduce the energy production cost per unit watt and to offer colored smart windows for building-integrated PVs, luminescent solar concentrators (LSCs) were explored as promising technology to exploit the sunlight absorption in semi-transparent windows, to improve the sunlight energy harvesting and to reduce the use of PV materials [6–10].

A typical luminescent solar concentrator (LSC) consists of an optical waveguide (e.g. glass or transparent polymer) embedded with down-shifting (or up-converting) fluorophores, which absorb sunlight radiation and re-emit photons in a longer (or shorter) wavelength range. Some of these photons are then guided by total internal reflection (TIR) and absorbed by the PV cells positioned at the edges of the LSCs [11,12]. When the LSC surface area is larger than its edge area, and the PCE of the device is sufficiently high ( $> 6\%$ ), the use of an LSC can reduce the cost of electricity per watt compared with that of standard PVs from silicon solar panels [13].

Recently, colloidal quantum dots (QDs) have been widely used as emitters in LSCs due to their size/composition tunable absorption/emission spectra, high fluorescence quantum yield (QY), large absorption coefficient, and structure-engineered Stokes shift (defined as the energy gap between the first-excitonic absorption peak and the

\* Corresponding author. Division of Material Science, Department of Engineering Sciences and Mathematics, Luleå University of Technology, 971 87, Luleå, Sweden.

\*\* Corresponding author.

\*\*\* Corresponding author.

E-mail addresses: [yqwang@qdu.edu.cn](mailto:yqwang@qdu.edu.cn) (Y. Wang), [hgzhao@qdu.edu.cn](mailto:hgzhao@qdu.edu.cn) (H. Zhao), [alberto.vomiero@ltu.se](mailto:alberto.vomiero@ltu.se) (A. Vomiero).

<https://doi.org/10.1016/j.nanoen.2019.03.038>

Received 9 December 2018; Received in revised form 26 February 2019; Accepted 10 March 2019

Available online 15 March 2019

2211-2855/© 2019 Published by Elsevier Ltd.

emission peak) compared with conventional organic dyes and polymers [14–20]. Usually, the Stokes shift is a crucial parameter for the realization of large-area high-efficiency LSCs with suppressed reabsorption energy loss [12,21,22]. Several strategies have been proposed to eliminate reabsorption by increasing the Stokes shift, including the doping of QDs (e.g. Mn doped ZnSe [23]), the use of intra-gap QDs (e.g. CuInSeS [24]) and heterostructured QDs (e.g. CdSe/ZnS [16], PbS/CdS [17], CdSe/CdS [21,22] and PbSe/PbS [25]). In the heterostructured QDs, the energy separation between the absorption and emission spectra can be designed by confining the two processes to different parts of the heterostructure. So far, this is typically achieved by the growth of a thick CdS shell on CdSe core QDs (called “giant” QDs) [22]. LSCs based on “giant” CdSe/CdS QDs exhibit an external optical efficiency ( $\eta_{\text{opt}}$ , defined as the ratio between the optical power of re-emitted photons reaching the edges of an LSC and the optical power of incident photons) of 1% with a lateral size of  $1.3 \times 21.5 \text{ cm}^2$  [22]. Unfortunately, a pronounced trade-off exists between the shell thickness and the QY in CdSe/CdS QDs, which affects the optical efficiency of their application in the LSCs [21,22]. It is necessary to understand the correlation between the crystal structure of QDs and their QY, aiming at preparing core/shell QDs with high QY, wide absorption spectrum and large Stokes shift.

In addition to the effect of fluorophores themselves, the geometry of the LSCs has a great influence on the  $\eta_{\text{opt}}$  of these devices. In order to increase the  $\eta_{\text{opt}}$  of the LSCs, the use of tandem structure (multiply-stacked waveguides) is an efficient approach. For example, tandem thin-film LSCs based on organic dyes (stacking two layers of LSCs fabricated by depositing a thin film of organic dyes on high-refractive-index glass substrates) exhibit a PCE of 7.1% (with a diffusive back reflector) with active area less than  $25 \text{ cm}^2$  [26,27]. The tandem LSCs based on inorganic fluorophores have recently been investigated. Wu et al. [28] demonstrated a large-area ( $> 230 \text{ cm}^2$ ) tandem LSC based on  $\text{Mn}^{2+}:\text{CdZnS}/\text{ZnS}$  QDs and  $\text{CuInSe}_2/\text{ZnS}$  QDs with a PCE of 3.1%. The  $\eta_{\text{opt}}$  up to 1.1% was also reported for a tandem LSC based on colloidal carbon dots [29]. Zhao et al. [30] investigated the tandem LSCs based on carbon dots and perovskite QDs, and they obtained a  $\eta_{\text{opt}}$  of ~3%. In our previous work, we described a tandem LSC based on carbon dots and CdSe/CdS QDs to enhance the efficiency and photo-stability of the single layer LSCs [31].

Compared to single junction LSCs, the tandem LSC can absorb more sunlight and boost the  $\eta_{\text{opt}}$  of the LSCs. However, the materials/fabrication cost for tandem LSC is higher than that for a single junction LSC, and the tandem structure often requires more space for installation. Another important issue where the tandem configuration might play a role is the long-term stability of the LSCs as the QDs are sensitive to surrounding environments, such as oxygen, humidity, alkalinity and other ambient environments. Indeed, a multi-layered configuration with stable materials might protect the QDs in the LSCs. Finally yet importantly, the efficiency of an LSC is critically affected by reabsorption processes and PL quenching due to the defects in the polymer matrix. Replacing traditional LSCs based on QDs/polymer with thin-film structure LSCs on a glass substrate can enhance the light trapping as most of the light transports in the high-quality glass, where the transport efficiency should be higher due to the lack of optical impurities and reabsorption (since there is no luminophores in it). When the luminophores dispersed in polymer are sandwiched between two sheets of glass, the optical loss for the device can be decreased and the long-term stability may be increased as the glass is typically acting as waveguide and protective layer. By considering the issues discussed above, Sol et al. [32] reported sandwich structure LSCs using  $5 \times 5 \text{ cm}^2$  indium tin oxides coated planar alignment cells filled by dye mixtures in a liquid crystal, and obtained a  $\eta_{\text{opt}}$  of 3.2%. Li et al. [33] also prepared similar three-layer structure of LSCs, polymethyl methacrylate (PMMA)/N-doped C-dots/PMMA film/glass structure, to obtain  $\eta_{\text{opt}}$  of 4.75% ( $2.5 \times 1.6 \text{ cm}^2$ ) and excellent photo-stability. To our best knowledge, until now there is only one report for the sandwich structure LSC based on colloidal QDs

[13]. That is the glass/CuInS<sub>2</sub>/ZnS QDs/polymer interlayer/glass device ( $10 \times 10 \text{ cm}^2$ ) with the thickness of QDs/polymer of 750–2300  $\mu\text{m}$ , exhibiting a  $\eta_{\text{opt}}$  of 8.1% (with a mirror) [13].

In this work, the sandwich structure LSC was designed and fabricated, which consists of glass/“giant” QDs-polymer thin film/glass with an interlayer (QDs-polymer film) thickness of 300–500  $\mu\text{m}$ . The “giant” QDs chromophores were core/shell CdSe/CdS QDs, synthesized via a hot-injection approach and a successive ionic layer adsorption and reaction (SILAR) method. The “giant” configuration was chosen for the QDs, because the core is still under quantum confinement, while the thick shell (shell thickness  $> 1.5 \text{ nm}$ ) endows the QDs very large Stokes shift and excellent stability, compared to bare or core/thin shell QDs. The as-fabricated large-area ( $100 \text{ cm}^2$ ) sandwich structure LSC based on CdSe/CdS QDs exhibits a  $\eta_{\text{opt}}$  of 2.95% under one sun illumination. This represents a 78% enhancement in efficiency over single layer LSC based on CdSe/CdS QDs fabricated under the same conditions. The improvement of  $\eta_{\text{opt}}$  for sandwich LSC is mainly due to the decrease of geometric (G) factor (the ratio of the top surface area of the LSC and the area of the LSC coupled with the PV cells) and photon escape. With further optimization, the sandwich structure LSCs have the potential to realize net-zero power consumption for modern cities by offering safe and low-cost seamless integration of energy production into the buildings.

## 2. Experimental section

### 2.1. Synthesis of CdSe/CdS QDs

CdSe QDs were synthesized by a hot injection approach. Then the QDs were coated with CdS shell by a SILAR method. The detailed description of the synthetic approach is shown in the Supporting Information (S.I.).

### 2.2. Preparation of the sandwich structure LSCs based on CdSe/CdS QDs

The CdSe/CdS QDs dispersed in toluene were mixed with polystyrene (PS) polymer with a final PS content of 2.5 wt%. The concentration of QDs in PS polymer is around 5.5 wt% (Fig. S1). Then the mixture was dropwise added on a glass substrate forming QDs film with a thickness of 300–500  $\mu\text{m}$  by drop casting method. The film is also spin-coated on the glass substrate. The coating process was conducted at 500 r.p.m for 30 s and then 1000 r.p.m for 30 s with an accelerating speed of 500 r.p.m. This process was repeated several times (3–5), to reach the desired thickness of the QDs/polymer layer. The surface roughness of the film is about 50 nm (Fig. S2), which was measured by atomic force microscopy (AFM). The glass dimensions are  $5 \times 5 \times 0.2 \text{ cm}^3$ ,  $5 \times 5 \times 0.4 \text{ cm}^3$ ,  $10 \times 10 \times 0.2 \text{ cm}^3$  and  $10 \times 10 \times 0.4 \text{ cm}^3$ . The sandwich structure LSCs were prepared by putting the glass on the thin-film glass. To avoid the effect of the air between the glass and QDs film, sandwich structure LSCs were also fabricated by stacking two unseasoned thin-film LSCs with half QDs concentration for each film and forming glass/film/glass structure.

### 2.3. Characterizations of CdSe/CdS QDs

X-ray diffraction (XRD) analysis was performed by a Rigaku Ultima IV X-ray diffractometer using a Cu-K $\alpha$  radiation source ( $\lambda = 0.15418 \text{ nm}$ ) with a step scan of  $2^\circ$ . Transmission electron microscopy (TEM) and high-resolution TEM (HRTEM) measurements were carried out using a JEOL JEM 2100Plus TEM operating at 200 kV. The energy-dispersive X-ray spectroscopy (EDS) was used to measure the content of elements presented in QDs samples. Thermogravimetric analysis (TGA) was carried out in a flow of nitrogen at  $10^\circ \text{C}/\text{min}$  using a TG209F3 TGA (Netzsch). AFM images from top surface of QDs/polymer film were obtained by AFM NT-MDT Prima, Bruker Dimension Edge. The scan area was  $10 \times 10 \mu\text{m}^2$ . Absorption spectra were recorded using a double beam Agilent Cary-5000 UV-Vis-NIR spectrophotometer in air equilibrated toluene. Steady state and time-resolved

photoluminescence (PL) characterization of the same solutions was performed on an Edinburgh FLS980 single photon counting fluorometer. PL quantum yield (QY) was measured with De Mello method by employing a polytetrafluoroethylene (PTFE) coated integrating sphere [34].

#### 2.4. Optical measurement of LSCs

Absorption and PL characterization was carried out with the same facilities employed for the solution-phase QDs characterization, equipped with a solid-state sample holder. Excitation-distance dependence PL spectra were collected by fixing the position of one LSC edge facing the detector, and excitation perpendicular to the LSC top-side with a movable laser ( $\lambda_{\text{ex}} = 450 \text{ nm}$ ).

The optical efficiency of the LSCs based on CdSe/CdS QDs was measured by using a solar simulator (Newport) at AM 1.5G (100 mW/cm<sup>2</sup>). During measurements, the optical power meter (Newport Model 843-R) was directly coupled on one side of LSC edges without using any optical devices (mirrors or fibers).

The  $\eta_{\text{opt}}$  of LSCs is calculated as the ratio of the output power ( $P_{\text{out}}$ ) coming out of the edges and the input power ( $P_{\text{in}}$ ) coming in through the top surface of the LSCs [35].

$$\eta_{\text{opt}} = \frac{P_{\text{out}}}{P_{\text{in}}} \quad (1)$$

When characterizing the optical performance of an LSC with a PV cell attached,  $\eta_{\text{opt}}$  can be defined as [35]:

$$\eta_{\text{opt}} = \frac{I_{\text{LSC}}}{I_{\text{SC}} \times G} \quad (2)$$

where  $I_{\text{LSC}}$  and  $I_{\text{SC}}$  are the short circuit current from the PV cells coupled with the LSC and from the same PV cell under direct illumination. For the optical efficiency measurement, the G factor is varied with different samples.

#### 2.5. Analytical model for efficiency of LSC

Following the formalism development elsewhere, the external efficiency of the LSC can be expressed as [8,35]:

$$\eta_{\text{external}} = \eta_{\text{abs}} \eta_{\text{internal}} \quad (3)$$

in which  $\eta_{\text{abs}}$  is the sunlight absorptance and  $\eta_{\text{internal}}$  is the internal efficiency.

$\eta_{\text{abs}}$  can be calculated as:

$$\eta_{\text{abs}} = (1 - R) \frac{\int_{E_g}^{\infty} S_{\text{in}}(\lambda)(1 - e^{-\alpha(\lambda)d})d\lambda}{\int_{E_g}^{\infty} S_{\text{in}}(\lambda)d\lambda} \quad (4)$$

in which  $\alpha$  is the absorption coefficient,  $S_{\text{in}}$  is the Sun irradiance and  $R$  is the reflection coefficient, that can be calculated as follows:

$$R = \frac{(n_{\text{glass}} - n_{\text{air}})^2}{(n_{\text{glass}} + n_{\text{air}})^2} \quad (5)$$

For the glass/air interface,  $R = 4\%$ .

Since our experimental data on the external optical efficiency have been obtained under a simulated solar light with non-monochromatic spectrum, we used a spectrally averaged internal efficiency over the PL emission of the QDs  $S_{\text{PL}}(\lambda)$ , calculated as:

$$\eta_{\text{internal}} = \frac{\int_0^{\infty} \frac{\eta_{\text{PL}} \eta_{\text{TIR}}}{1 + \beta \alpha(\lambda)L(1 - \eta_{\text{PL}} \eta_{\text{TIR}})} S_{\text{PL}}(\lambda) d\lambda}{\int_0^{\infty} S_{\text{PL}}(\lambda) d\lambda} \quad (6)$$

in which  $S_{\text{PL}}(\lambda)$  is the PL emission spectrum,  $\eta_{\text{PL}}$  is the estimated QY of the QDs,  $\eta_{\text{TIR}}$  is the total internal reflection efficiency of the waveguide that can be estimated to be around 75%, and  $\beta$  is a numerical value fixed to 1.4 and  $L$  is the length of the LSC.

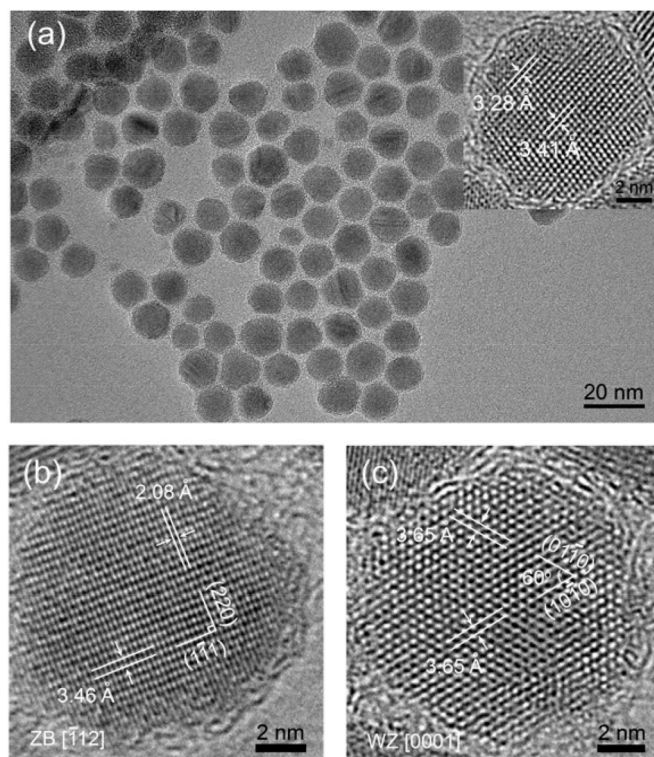


**Fig. 1.** TEM (a) and HRTEM images (b, c) of the CdSe/15CdS QDs with the shell growth at 240 °C.

### 3. Results and discussion

#### 3.1. Synthesis and structure of CdSe/CdS QDs

The CdSe QDs were first synthesized *via* a hot injection approach. The CdSe core QDs show highly crystalline structure with a diameter of 3.3 nm, as shown in Figs. S3a and b. Then, the CdS thick shell was covered around the core *via* a SILAR approach, producing a “giant” QD. TEM image (Fig. 1a) shows that the QDs exhibit a uniform spherical or hexagonal shape. The diameter of the as-synthesized QDs ranges from 9 nm to 16 nm, with an average diameter of 12.1 nm indicating that the shell thickness is around 4.4 nm after the growth of 15-monolayer CdS, when the reaction temperature is 240 °C (Fig. S3). Inset in Fig. 1a is the HRTEM image of an individual QD at the CdS injection temperature of 240 °C. The lattice spacing measured from the core region is larger than that from the edge region indicating the core/shell structure of the CdSe/CdS QDs. This is because the lattice parameter of CdSe (cubic  $a = 6.077 \text{ \AA}$ , JCPDS: 00-019-0191) is larger than that of CdS (cubic  $a = 5.82 \text{ \AA}$ , JCPDS: 00-001-0647). When the CdS shell is grown epitaxially on the CdSe core, the shell layer tends to mimic the crystalline characters of the core. As the thickness of the shell layer increases, the influence of the core on lattice spacing decreases and the shell tends to maintain its intrinsic characters. Thus, the lattice spacing at the core region is larger than that at the edge region. To further identify this crystallization, the CdSe/CdS QDs with other reaction parameters (*e.g.* shell growth temperature) were synthesized. At the reaction temperature of 200 °C, the CdSe/CdS QDs have a quasi-pyramidal shape (Fig. S4). HRTEM image in Fig. S4a demonstrates the core/shell structure of the QDs, which is similar to the inset in Fig. 1a. The EDS reveals the presence of elemental Cd, Se and S (Fig. S5). Except for the change of the lattice parameter and element types, the change of the crystal structure can also indicate the temperature-dependent crystallization of the QDs, which can be confirmed by XRD patterns.

From the XRD patterns in our previous report, the core CdSe QDs have a zinc-blende (ZB) crystal structure [31], while the CdSe/CdS

core/shell QDs have a structure with two phase components: ZB and wurtzite (WZ) (Fig. S6). When the CdS shell grows at 200 °C, the ZB/WZ ratio is 1:1. As the reaction temperature increases to 240 °C, the predominant phase is WZ (ZB/WZ ratio is 1:4). This indicates that the stable thermodynamic structure of the CdS shell is the WZ phase, consistent with the previous reports [36,37]. At high reaction temperature (240 °C), the shell growth might be expected to achieve the more stable thermodynamic phase (WZ) rather than the ZB phase. The structure of these QDs can be further confirmed by HRTEM images. Figs. 1b and c shows typical HRTEM images of the synthesized QDs with shell growth temperature of 240 °C. In Fig. 1b, the particle was viewed along [112] zone axis. The measured lattice spacing of two perpendicular planes is 2.08 Å and 3.46 Å, corresponding to (220) and (111) planes of ZB structure of CdS. In addition to the crystal structure of ZB phase, the WZ structure of QDs was also observed in HRTEM images, as shown in Fig. 1c. The measured lattice spacings of 3.65 Å and 3.65 Å with an angle of 60° between the two planes are well consistent with the (1010) and (0110) planes of the CdS WZ structure, suggesting that the particle is viewed along [0001] direction. Similar to the CdS shell grown at 240 °C, when the core CdSe QDs are covered with CdS shell at 200 °C, both ZB and WZ crystal structure of the QDs can be observed in the HRTEM image (Figs. S4b–e), but more QDs exhibit ZB structure, which is consistent with the XRD analyses (Fig. S6).

### 3.2. Optical properties of QDs

The absorption and emission spectra of the CdSe QDs and CdSe/CdS QDs are shown in Fig. S7 and Fig. 2a, respectively. CdSe QDs have the first excitonic absorption peak at 536 nm and the emission peak at 574 nm (Fig. S7). After coating the core QDs with 15-monolayer CdS, the absorption and emission spectra of CdSe/15CdS QDs are dominated by the optical features of the shell, due to the larger shell volume compared to the core (volume ratio of shell and core is ~48:1), as shown in Fig. 2a. The CdSe/CdS QDs absorb the sunlight in the range from 300 nm to

500 nm, corresponding to the CdS bandgap ( $E_g$ , 2.49 eV [38]), matching well with the Sun's spectrum in the ultraviolet (UV) and visible range. The excitation spectrum reflects the absorption spectrum (Fig. S8), proving there is a complete overlap of these two spectra. The PL peak of core/shell QDs shows a typical red shift (~50 nm) with respect to the core QDs due to the leakage of electron from the core to the shell [36] (Fig. 2a and S7). Compared to CdSe core QDs, the blue shift of absorption peak and red shift of PL peak for CdSe/CdS core/shell QDs indicate that the growth of CdS shell can increase the Stokes shift (~150 meV vs. ~500 meV). The PL spectrum of QDs synthesized at 200 °C is slightly red-shifted compared to that of QDs synthesized at 240 °C. This is due to the asymmetric e-h wavefunction in pyramidal structure [39]. The QYs of the CdSe/CdS QDs with shell growth at 200 °C and 240 °C are 7.9% and 38.4%, respectively, which were calculated by means of an integrating sphere ( $\lambda_{ex} = 450$  nm) coupled in a PL spectroscopy. Usually, higher QY in QDs indicates that the QDs have a better surface passivation with less surface recombination centers [40,41]. To understand the nature of the QY in the QDs with different morphologies, we measured the PL lifetime of QDs, as shown in Fig. 2b and Table 1. The PL decay curves were well fitted by a tri- or double-exponential function, and the average lifetime ( $\tau_{avg}$ ) is calculated by the following equation:

$$\tau_{avg} = \frac{A_1 \tau_1^2 + A_2 \tau_2^2 + A_3 \tau_3^2}{A_1 \tau_1 + A_2 \tau_2 + A_3 \tau_3} \quad (7)$$

where  $A_x$  ( $x = 1, 2, 3$ ) are the fitting coefficients of the PL decay and  $\tau_x$  ( $x = 1, 2, 3$ ) are the characteristic lifetimes, respectively. The average lifetimes of the CdSe/CdS QDs grown at 200 °C and 240 °C were calculated to be 32.8 ns and 50.1 ns, respectively. The measured lifetime is equal to that reported in Ref. [12]:

$$\tau_{avg} = \frac{1}{\kappa_r + \kappa_{nr}} \quad (8)$$

where  $\kappa_r$  and  $\kappa_{nr}$  are the radiative and the non-radiative decay rate in QDs, respectively.  $\kappa_r$  and  $\kappa_{nr}$  can also be used to calculate the QY with the

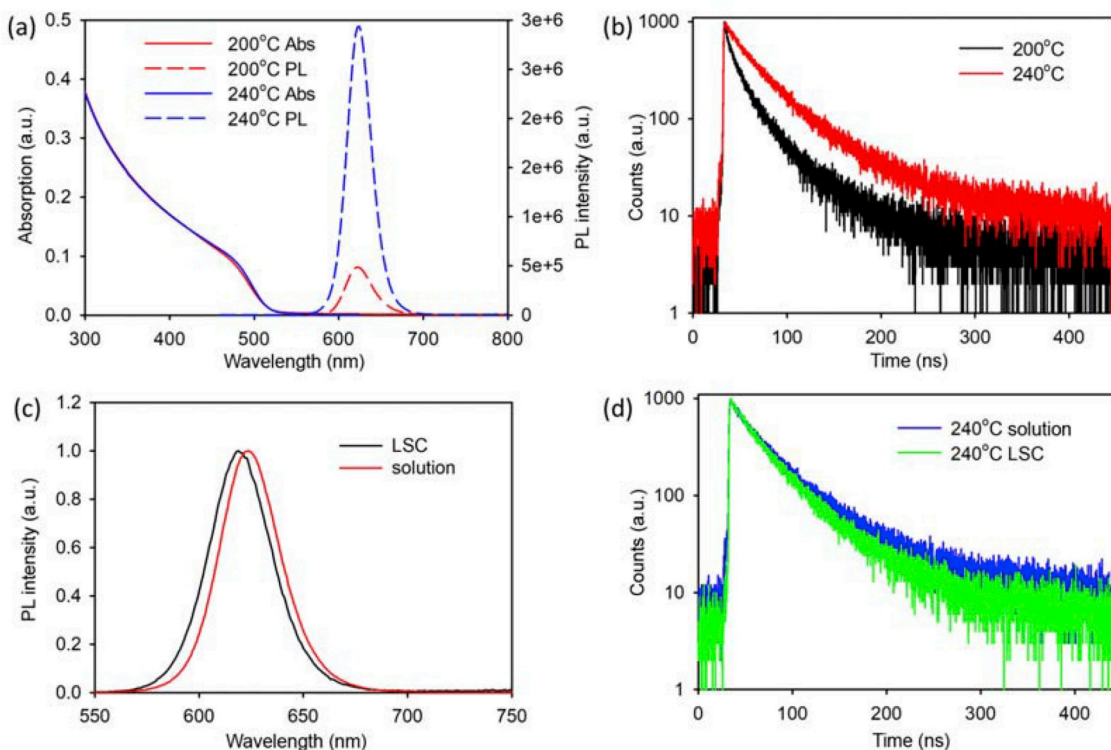


**Fig. 2.** (a) Absorption and PL spectra of the CdSe/CdS QDs in toluene. (b) PL decay curves of the CdSe/CdS QDs with the shell growth at 200 °C and 240 °C ( $\lambda_{ex} = 455$  nm,  $\lambda_{em} = 620$  nm). (c) PL spectra of the CdSe/CdS 240 °C QDs in toluene and LSC. (d) PL decay curves of the CdSe/CdS 240 °C QDs in toluene and the LSC.

**Table 1**

Optical parameters of the CdSe/CdS QDs with the shell growth at 200 °C (#1), 240 °C (#2) and #2 QDs in LSCs, respectively.

Samples	QY (%)	A <sub>1</sub>	τ <sub>1</sub> (ns)	A <sub>2</sub>	τ <sub>2</sub> (ns)	A <sub>3</sub>	τ <sub>3</sub> (ns)	τ <sub>avg</sub> (ns)	κ <sub>r</sub> (ns <sup>-1</sup> )	κ <sub>nr</sub> (ns <sup>-1</sup> )
#1	7.9	0.41	4.5	1.50	20.9	0.07	69.2	32.8	2.4 × 10 <sup>-3</sup>	0.28 × 10 <sup>-3</sup>
#2	38.4	–	–	0.73	26.5	0.26	73.8	50.1	7.7 × 10 <sup>-3</sup>	0.12 × 10 <sup>-3</sup>
#2 in LSC	36.2	–	–	0.67	24.7	0.32	57	41.6	8.7 × 10 <sup>-3</sup>	0.15 × 10 <sup>-3</sup>

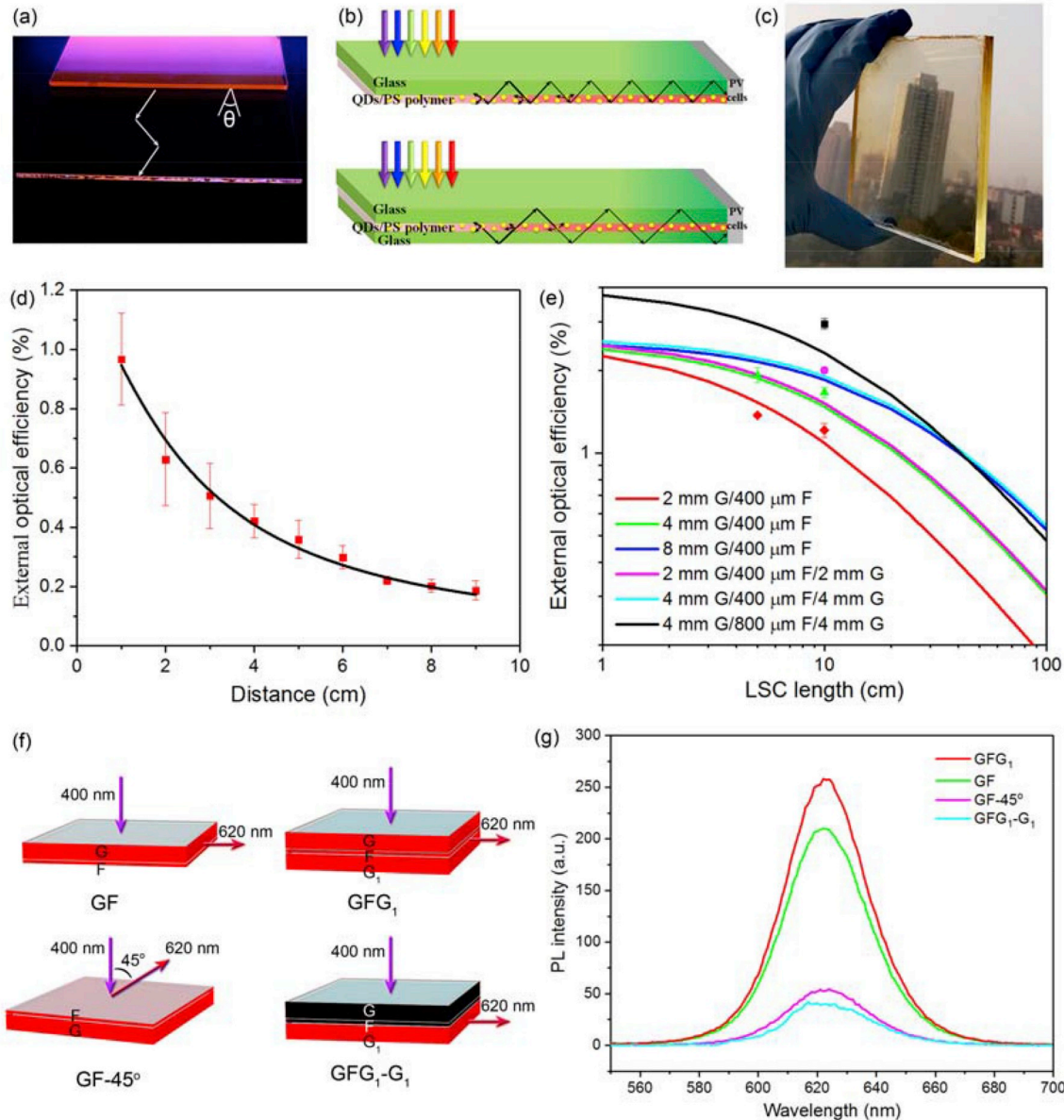


**Fig. 3.** (a) Photograph of the single layer LSC based on CdSe/CdS QDs under ultraviolet radiation. The bottom layer is a piece of glass. (b) Schematic diagram of single layer film LSC and sandwich structure LSC configurations. (c) Photograph of the sandwich structure LSC based on CdSe/CdS QDs. (d) Optical efficiency of CdSe/CdS QD-based LSCs as a function of distance from the side edge. The illumination area is  $10 \times 1 \text{ cm}^2$ . (e) Analytical model of the performance of the different LSCs based on CdSe/CdS QDs. External optical efficiency of LSCs under one sun illumination, with the experimental absorption and PL QY. The points are the experimental data obtained with the power meter. “G” and “F” represent the glass and QDs film, respectively. (f) Schematic diagram of PL measurements of single and sandwich structure LSCs and the results (g).

following equation [12]:

$$QY = \frac{\kappa_r}{\kappa_r + \kappa_{nr}} \quad (9)$$

Based on the above-mentioned equations (7)–(9), we calculated the radiative decay rate and nonradiative decay rate to make a simple comparison between the two QDs. For the CdSe/CdS QDs synthesized at

200 °C, the calculated  $\kappa_{nr}$  is  $0.028 \text{ ns}^{-1}$ , while for the CdSe/CdS QDs synthesized at 240 °C,  $\kappa_{nr}$  decreases to  $0.012 \text{ ns}^{-1}$ . As the  $\kappa_{nr}$  is mainly induced by the surface chemical states [17,40], the higher  $\kappa_{nr}$  in quasi-pyramidal CdSe/CdS QDs, the higher the density of surface defects/traps is. In fact, compared to spherical QDs, in the pyramidal QDs, the e-h wavefunctions can spread into the surface of QDs, resulting in the threefold lower  $\kappa_r$  in QDs synthesized at 200 °C (Table 1). Thus, the

pyramidal QDs are more sensitive to the surrounding environments and higher density of surface defects/traps is expected compared with spherical CdSe/CdS QDs.

### 3.3. Fabrication and optical properties of LSCs

The thin-film LSCs were fabricated by drop casting method with the well-dispersed QDs/PS polymer solution (the details can be found in the experimental section). The QY of the QDs is one of the critical factors that need to be considered for achieving high LSC efficiency, thus the CdSe/CdS QDs with the shell growth at 240 °C were used to prepare LSCs. To further demonstrate the effectiveness of the deposition method, the PL spectra of CdSe/CdS QDs dispersed in toluene and LSCs are displayed in Fig. 2c. The PL spectrum of QDs in the LSC is very similar to that in solution, with a small shift in the PL maximum from 624 nm to 619 nm, which might be due to the different environment surrounding the QDs and the different dielectric constants. A considerable reduction in optical losses can be investigated by the study of PL intensity as a function of the propagation length in the LSCs, as shown in Fig. S9. In LSCs, the PL intensity typically drops with increasing distance from the illumination point (Fig. S9b). Aside from the geometrical motivation for this decrease of PL intensity, both photon escape and reabsorption energy losses contribute to the further decrease of PL intensity. The normalized PL spectra are shown in Fig. S9c. Fig. S9d plotted the PL peak position as a function of optical paths. The change in the PL spectra with respect to the full width at half maximum and peak position can occur only when the spectral distortion caused by light reabsorption of the QDs takes place [6,24]. In our case, by increasing the optical path, the PL spectra of QDs exhibit a relatively stable peak position and peak width indicating the lack of reabsorption losses due to the efficient separation between the absorption and emission spectra. The QY of the QDs in the LSC is very close to that in solution, indicating the stability and the effectiveness of the deposition method. The PL decay curves of the QDs both in LSC and solution are very similar (Fig. 2d). They can be characterized by two lifetimes with similar pre-exponential factors, but the longer lifetime shifts from 73.8 to 57.0 ns upon embedding in the thin film (Table 1), proving that this long-lived state is slightly affected by the different environments.

Fig. 3a shows a LSC film under UV light, with a piece of glass placed on the bottom of the LSC. It can be seen that some of the re-emitted light escaped from the film surface, and then was reflected by the bottom layer. Thus, sandwich structure LSC by stacking two film LSCs was prepared to improve the efficiency of the LSC. The glass also serves as a protective layer to isolate the effects of ambient environment (atmosphere, humidity and acidity-alkalinity) on QDs film layer. The specific schematics of a typical single layer film LSC and sandwich structure LSC are demonstrated in Fig. 3b. As shown in the case of sandwich structure LSCs, compared to single junction LSC, lower propagation within the QDs film might be expected, reducing reabsorption losses contribution to the LSC optical efficiency, which allows to realize large-area, high efficiency LSCs. In Fig. 3c, a sample of sandwich structure LSC with high transmissivity is presented. Demonstrations of the LSC under ambient and UV light conditions are also given in Fig. S10. A clear concentrated red light can be seen from the edges when the top surface of the LSC is placed under a UV light, indicating the promising potential to be used in power buildings.

For a quantitative study of the performance of LSCs based on CdSe/CdS QDs, the square-shaped glasses with thickness of 2 mm and 4 mm and top surface area of 100 cm<sup>2</sup> were used. Fig. 3d illustrates the optical efficiency, calculated by equation (1), for LSC with different illumination distances from the side edges. In general, increasing the distance reduces the optical efficiency due to the enhancement of several loss processes. Since we observed negligible reabsorption in our QDs, the optical efficiency decay is likely due to the decrease of collection angle, as the measurement is performed by collecting the light from a single side. During measurements, the photodetector is placed at a single lateral side, and the excitation light is fixed, only changing the distance between irradiation spot by masking the LSC. With this measurement configuration, by increasing the distance

between irradiation spot and detection side, the probability of collecting photons directly emitted by the luminophore decreases, therefore the photons collected are most likely affected by multiple reflection processes within the waveguide and suffer from increased probability of optical losses such as scattering, matrix absorption and surface escape.

Using an analytical model of planar LSCs, we can predict the efficiency of large-area LSCs and also simulate the influence of different parameters, such as the thickness of the LSCs on the  $\eta_{\text{opt}}$  of LSCs. As shown in Fig. 3e, using the value of the QY close to the experimental one, the analytical model fits nicely the experimental data of the single layer (red and green lines). In this figure, glass and QDs film layers are labeled as “G” and “F”, respectively. The detailed measurement of the optical efficiency for the LSCs is shown in experimental section 2.4. Although the experimental points for the sandwich system (black and pink dots) deviate from the theoretical model, the experimental value is within 18% of the theoretical value and follows the same trend. In Fig. 3e, we can see the effect of the length of the LSCs on the  $\eta_{\text{opt}}$  under one sun illumination. It also shows the beneficial effect of employing the sandwich structure. By comparing with the single layer structure, the LSC with sandwich structure maintains a higher  $\eta_{\text{opt}}$  due to the reduction of the G factor and photon escape, and the enhancement of absorption (Fig. 3e). The single layer LSC based on CdSe/CdS QDs shows a  $\eta_{\text{opt}}$  of 1.66% when the G factor is 6.25 ( $10 \times 10 \times 0.4 \text{ cm}^3$ ). This value is increased over 38% compared with the highest values reported in the literature for a similar system with CdSe/CdS QDs (Table S1) [12,22]. This improvement with single layer film structure can be explained via the reduction of the reabsorption loss when the light propagates in the glass (Fig. 3b). In the sandwich structure LSC based on CdSe/CdS QDs with the G factor of 6.25 ( $10 \times 10 \times 0.4 \text{ cm}^3$ ), the  $\eta_{\text{opt}}$  reaches 2.02%, with an enhancement of ~22% compared to the single layer LSC. This may be attributed to the fact that the some scattered light from the uneven film surface was collected by the bottom glass layer. In Fig. 3e, we explored the case of increasing light absorption, i.e. from 9% (colored lines) increase to 13.7% (black line), for the LSC. As expected, before reaching saturated absorption of the QDs, as the content of QDs increases, the LSC absorbs more sunlight and the  $\eta_{\text{opt}}$  increases. However, due to the increase of QDs content, the reabsorption loss increases and the  $\eta_{\text{opt}}$  decreases faster as the area increases. The enhanced  $\eta_{\text{opt}}$  of sandwich structure LSC can also be demonstrated by the increase of integrated PL intensity. As shown in Figs. 3f and g, the PL emission peak of the sandwich structure LSCs shows stronger PL intensity than the single layer LSCs. The PL intensity was determined by the quantity of photon numbers with uniform intensity excitation beam at wavelength of 400 nm (the same emission slit width and excitation slit width) [42]. From Figs. 3f and g, we can see that the maximum emission peaks of the LSCs are all at 622 nm under an excitation wavelength of 400 nm. The PL intensity of the sandwich structure LSC (red line) increased 24% compared to that of the single thin-film LSC (green line), which is consistent with the improvement of the efficiency for LSCs. The enhanced PL intensity of LSCs with the addition of glass at the surface of thin-film LSCs demonstrates the effectiveness of the sandwich structure LSCs in the improvement of the optical properties.

The sandwich structure LSCs based on CdSe/CdS QDs have a maximum  $\eta_{\text{opt}}$  of 2.95% with an increase of 78% compared with single layer LSCs. This efficiency is 2.5 times higher than that of the traditional single layer LSCs based on CdSe/CdS QDs reported previously (LSC dimension:  $7 \times 1.5 \times 0.3 \text{ cm}^3$ ) [12]. No significant difference can be found in the  $\eta_{\text{opt}}$  measured by optical power meter or silicon solar cell. We further measured the solar-to-electrical power conversion efficiency (PCE) using edge-coupled monocrystalline silicon solar cell (Fig. S11). The sandwich and single layer LSCs deliver PCEs of 2.25% and 1.26%, respectively. This means that the sandwich configuration allows for 79% PCE boost compared to single layer LSC, which matches well with the improvement of the  $\eta_{\text{opt}}$ .

Using this sandwich strategy, we also fabricated a series of LSCs based on CdSe and CdSe/CdS QDs with different shell thickness in order to study the influence of shell thickness on the device efficiency. The absorption/PL spectra of the CdSe show the first excitonic peak near 550 nm and the

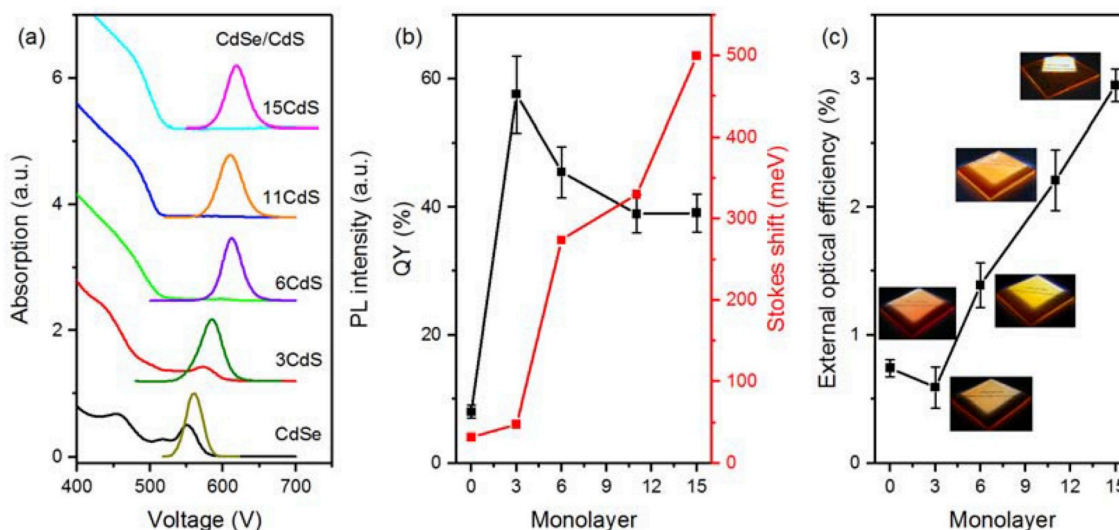


**Fig. 4.** (a) Absorption and PL spectra of CdSe QDs before and after coating with different cycle of CdS shell layers. (b) The variation of the QY and Stokes shift during the growth of CdSe/CdS QDs. (c) External optical efficiency of as-fabricated LSCs ( $10 \times 10 \text{ cm}^2$ ) based on CdSe and CdSe/CdS QDs with different shell thickness.

emission peak near 560 nm. By coating the CdSe with several monolayers of CdS, the absorption and PL spectra were tunable (Fig. 4a). Coating the CdSe QDs with three monolayers of CdS, no obvious changes can be seen in Stokes shift, but for the giant core/shell QDs, when the number of shell layer increases, the Stokes shift of the core/shell QDs increases (Fig. S12b). In addition, when the CdSe core is covered with 3-monolayer CdS shell, the QDs have significantly enhanced QY. Further growth of the CdS shell results in a decrease of QY (from  $\sim 60\%$  to  $40\% \sim 50\%$ ), but overall, it is still quite high compared to bare CdSe QDs (8%) due to the improved surface passivation. Fig. 4c shows the efficiencies of the LSCs with different cycles of shell coating. The efficiency for the CdSe QDs based LSC is 0.74%, due to the strong overlap of absorption and PL spectra, which makes the CdSe QDs unsuitable for the LSCs (Fig. 4a). Due to the surface defects, the CdSe QDs are not stable and the QY is very sensitive to the surrounding environments. For the CdSe/3CdS QDs based LSC, due to the small Stokes shift, the efficiency is still low. When the number of shell layers increases, the efficiency for the CdSe/CdS LSCs is improved due to the increased Stokes shift. The detailed effect of Stokes shift on LSC efficiency is further characterized by the PL intensity as shown in Fig. S12. In general, the PL intensity decreases with the increase of optical path for LSCs due to the reabsorption energy losses. For the LSCs based on CdSe/xCdS QDs ( $x = 0, 3, 6, 11$ ), with the shell thickness increases (Stokes shift increase), the reabsorption loss decreases, leading to lower decrease of the PL intensity.

For the sandwich structure LSCs, the incident light propagates in different pathways, as shown in Fig. S13a. As the refractive index of QDs/polymer matrix ( $n_{\text{polymer}}$ ) is measured to be  $\sim 1.58$ , which is higher than that of glass ( $n_{\text{glass}}$  measured to be 1.51), the emitted light can refract to glass with various angles ( $< 73^\circ$ ). Part of the light will be refracted to the glass layers and some of light will be trapped in the QDs/polymer due to total internal reflection (Fig. S13). In such LSC structure, the ratio of photons lost from the top-side of the LSC, due to the escape cone at the glass/air interface, will be driven by the refractive index of glass, other than polymer. In fact, some re-emitted light is still totally transported inside the QDs/polymer layer, as the refractive index of polymer is larger than that of glass. The total reflection efficiency ( $\eta_{\text{TIR}}$ ) in QDs/polymer film can be estimated by the critical angle [12,43–45].

$$\eta_{\text{TIR}} = \sqrt{1 - \left(\frac{n_{\text{glass}}}{n_{\text{polymer}}}\right)^2}$$

When  $n_{\text{glass}} \geq n_{\text{polymer}}$ , there is no TIR in the QDs/polymer layer. When  $n_{\text{glass}} < n_{\text{polymer}}$ , the  $\eta_{\text{TIR}}$  curve in QDs/polymer film as a function

of polymer refractive index is shown in Fig. S13b (the refractive index,  $n$ , of glass is fixed to be 1.51). Although the efficiency of the LSCs in this case is lower than that of  $n_{\text{glass}} > n_{\text{polymer}}$ , it is still higher than the traditional polymer LSCs due to its lower reabsorption loss. The reflected light by glass derives from the escaped light of the film/glass interface and the light outside the absorption range of the QDs. While the presence of the glass has little effect on absorption of the LSCs, the propagation of light in pure glass will not cause reabsorption loss by the QDs, which can improve the efficiency of the large-area LSCs. In this case, the enhancement in the  $\eta_{\text{opt}}$  for sandwich structure LSCs over single-layer LSC can be attributed to the following effects: 1) the reabsorption energy loss in LSCs based on QDs, due to the spectral overlap of absorption and emission, can be mitigated by using the glass; 2) sandwich structure has 2-time lower G factor compared with a single layer LSC; 3) the untrapped light and escaped re-emitted light from the film surface can be collected by the external glass layers that reflect it back to film, enhancing the edge emission. In addition to improving the efficiency, the sandwich structure avoids the direct contact between the QDs film and ambient environment, which may enhance the stability and lifetime of the devices and reduce the environment pollution caused by Cd ion. After three-month storage, the  $\eta_{\text{opt}}$  of sandwich structure LSC drops only 15%, while for the single layer LSC, it drops more than 25%, which indicates that the sandwich structure can improve the stability of the devices. These results could shed light on the study of sandwich structure LSCs based on other optical waveguide materials. One promising future research direction is to select the optical waveguide material with optimized refractive index as the middle layer to further improve the efficiency of the sandwich structure LSCs.

#### 4. Conclusion

In summary, we synthesized “giant” CdSe/15CdS core/shell QDs with high QY and good stability by controlling shell growth temperature via the SILAR approach. These QDs were integrated into large-area sandwich structure LSCs, where a QDs/PS polymer film is sandwiched between two glass plates. The prototype LSC based on the CdSe/CdS core/shell QDs exhibits a PCE of 2.25% and a  $\eta_{\text{opt}}$  of 2.95%, which indicates an over 78% enhancement in efficiency with respect to the single layer film LSC, attributed to lower G factor and the decrease of reabsorption loss due to light propagation in the glass. The QDs film encapsulated between two pieces of glass reduces the interplay of LSCs and environment, and could improve the stability and practicability. Due to the high performance, easy preparation and low cost, QD-based

sandwich structure LSCs can provide a viable pathway to further reduce the cost of solar electricity, and supplement the existing PV technology by coupling the building windows and PV cells.

## Acknowledgements

H. Zhao acknowledges the start funding support from Qingdao University and the funding from the Natural Science Foundation of Shandong Province (ZR2018MB001). Y. Q. Wang would like to thank the financial support from the Top-notch Innovative Talent Program of Qingdao City (Grant No. 13-CX-8) and Qingdao International Center for Semiconductor Photoelectric Nanomaterials, and Shandong Provincial University Key Laboratory of Optoelectrical Material Physics and Devices. R.M. and A.V. acknowledge the Kempe Foundation, the Knut and Alice Wallenberg Foundation, the ÅForsk Foundation and the LTU Lab fund program for partial financial support.

## Appendix A. Supplementary data

Supplementary data to this article can be found online at <https://doi.org/10.1016/j.nanoen.2019.03.038>.

## References

- N. Arora, M.I. Dar, A. Hinderhofer, N. Pellet, F. Schreiber, S.M. Zakeeruddin, M. Grätzel, Perovskite solar cells with CuSCN hole extraction layers yield stabilized efficiencies greater than 20%, *Science* 358 (2017) 767–771.
- J. Qi, W. Zhang, R. Cao, Solar-to-hydrogen energy conversion based on water splitting, *Adv. Energy Mater.* 8 (5) (2018) 1701620.
- S. Chandra, M. Rafiee, J. Doran, S.J. McCormack, Absorption coefficient dependent non-linear properties of thin film luminescent solar concentrators, *Sol. Energy Mater. Sol. Cell.* 182 (2018) 331–338.
- M.K. Mat Desa, S. Sapeai, A.W. Azhari, K. Sopian, M.Y. Sulaiman, N. Amin, S.H. Zaidi, Silicon back contact solar cell configuration: a pathway towards higher efficiency, *Renew. Sustain. Energy Rev.* 60 (2016) 1516–1532.
- A. Louwen, W. van Sark, R. Schropp, A. Faaij, A cost roadmap for silicon hetero-junction solar cells, *Sol. Energy Mater. Sol. Cell.* 147 (2016) 295–314.
- H. Zhao, Y. Zhou, D. Benetti, D. Ma, F. Rosei, Perovskite quantum dots integrated in large-area luminescent solar concentrators, *Nano Energy* 37 (2017) 214–223.
- H.J. Song, B.G. Jeong, J. Lim, D.C. Lee, W.K. Bae, V.I. Klimov, Performance limits of luminescent solar concentrators tested with seed/quantum-well quantum dots in a selective-reflector-based optical cavity, *Nano Lett.* 18 (1) (2018) 395–404.
- H. Li, K. Wu, J. Lim, H.J. Song, V.I. Klimov, Doctor-blade deposition of quantum dots onto standard window glass for low-loss large-area luminescent solar concentrators, *Nature Energy* 1 (2016) 16157.
- J. Zhang, M. Wang, Y. Zhang, H. He, W. Xie, M. Yang, J. Ding, J. Bao, S. Sun, C. Gao, Optimization of large-size glass laminated luminescent solar concentrators, *Sol. Energy* 117 (2015) 260–267.
- C. Corrado, S.W. Leow, M. Osborn, E. Chan, B. Balaban, S.A. Carter, Optimization of gain and energy conversion efficiency using front-facing photovoltaic cell luminescent solar concentrator design, *Sol. Energy Mater. Sol. Cell.* 111 (2013) 74–81.
- F. Purcell-Milton, Y.K. Gun'ko, Quantum dots for luminescent solar concentrators, *J. Mater. Chem.* 22 (33) (2012) 16687–16697.
- H. Zhao, D. Benetti, L. Jin, Y. Zhou, F. Rosei, A. Vomiero, Absorption enhancement in “giant” core/alloyed-shell quantum dots for luminescent solar concentrator, *Small* 12 (38) (2016) 5354–5365.
- M.R. Bergren, N.S. Makarov, K. Ramasamy, A. Jackson, R. Guglielmetti, H. McDaniel, High-performance CuInS<sub>2</sub> quantum dot laminated glass luminescent solar concentrators for windows, *ACS Energy Lett.* 3 (3) (2018) 520–525.
- J. Bomm, A. Büchtemann, A.J. Chatten, R. Bose, D.J. Farrell, N.L.A. Chan, Y. Xiao, L.H. Slooff, T. Meyer, A. Meyer, W.G.J.H.M. van Sark, R. Koole, Fabrication and full characterization of state-of-the-art quantum dot luminescent solar concentrators, *Sol. Energy Mater. Sol. Cell.* 95 (8) (2011) 2087–2094.
- H. Lin, P. Xie, Y. Liu, X. Zhou, B. Li, Tuning luminescence and reducing reabsorption of CdSe quantum disks for luminescent solar concentrators, *Nanotechnology* 26 (33) (2015) 335401.
- B.A. Ebrahimpour, H.R. Askari, A.B. Ramezani, Investigation of linear optical absorption coefficients in core-shell quantum dot (QD) luminescent solar concentrators (LSCs), *Superlattice. Microsc.* 97 (2016) 495–505.
- Y. Zhou, D. Benetti, Z. Fan, H. Zhao, D. Ma, A.O. Govorov, A. Vomiero, F. Rosei, Near infrared, highly efficient luminescent solar concentrators, *Adv. Energy Mater.* 6 (11) (2016) 1501913.
- L. Tan, Y. Zhou, F. Ren, D. Benetti, F. Yang, H. Zhao, F. Rosei, M. Chaker, D. Ma, Ultrasmall PbS quantum dots: a facile and greener synthetic route and their high performance in luminescent solar concentrators, *J. Mater. Chem. A* 5 (21) (2017) 10250–10260.
- L.J. Brennan, F. Purcell-Milton, B. McKenna, T.M. Watson, Y.K. Gun'ko, R.C. Evans, Large area quantum dot luminescent solar concentrators for use with dye-sensitised solar cells, *J. Mater. Chem. A* 6 (6) (2018) 2671–2680.
- R. Mazzaro, A. Vomiero, The renaissance of luminescent solar concentrators: the role of inorganic nanomaterials, *Adv. Energy Mater.* 1801903 (2018) 1801903.
- I. Coropceanu, M.G. Bawendi, Core/shell quantum dot based luminescent solar concentrators with reduced reabsorption and enhanced efficiency, *Nano Lett.* 14 (7) (2014) 4097–4101.
- F. Meinardi, A. Colombo, K.A. Velizhanin, R. Simonutti, M. Lorenzon, L. Beverina, R. Viswanatha, V.I. Klimov, S. Brovelli, Large-area luminescent solar concentrators based on ‘Stokes-shift-engineered’ nanocrystals in a mass-polymerized PMMA matrix, *Nat. Photon.* 8 (5) (2014) 392–399.
- C.S. Erickson, L.R. Bradshaw, S. McDowall, J.D. Gilbertson, D.R. Gamelin, D.L. Patrick, Zero-reabsorption doped-nanocrystal luminescent solar concentrators, *ACS Nano* 8 (2014) 3461–3467.
- F. Meinardi, H. McDaniel, F. Carulli, A. Colombo, K.A. Velizhanin, N.S. Makarov, R. Simonutti, V.I. Klimov, S. Brovelli, Highly efficient large-area colourless luminescent solar concentrators using heavy-metal-free colloidal quantum dots, *Nat. Nanotechnol.* 10 (10) (2015) 878–885.
- U. Aeberhard, R. Vaxenburg, E. Lifshitz, S. Tomić, Fluorescence of colloidal PbSe/PbS QDs in NIR luminescent solar concentrators, *Phys. Chem. Chem. Phys.* 14 (47) (2012) 16223–16228.
- L.H. Slooff, E.E. Bende, A.R. Burgers, T. Budel, M. Pravettoni, R.P. Kenny, E.D. Dunlop, A. Büchtemann, A luminescent solar concentrator with 7.1% power conversion efficiency, *Phys. Status Solidi Rapid Res. Lett.* 2 (2008) 257–259.
- M.J. Currie, J.K. Mapel, T.D. Heidel, S. Goffri, M.A. Baldo, High-efficiency organic solar concentrators for photovoltaics, *Science* 321 (2008) 226–228.
- K. Wu, H. Li, V.I. Klimov, Tandem luminescent solar concentrators based on engineered quantum dots, *Nat. Photon.* 12 (2018) 105–110.
- Y. Zhou, D. Benetti, X. Tong, L. Jin, Z.M. Wang, D. Ma, H. Zhao, F. Rosei, Colloidal carbon dots based highly stable luminescent solar concentrators, *Nano Energy* 44 (2018) 378–387.
- H. Zhao, D. Benetti, X. Tong, H. Zhang, Y. Zhou, G. Liu, D. Ma, S. Sun, Z.M. Wang, Y. Wang, F. Rosei, Efficient and stable tandem luminescent solar concentrators based on carbon dots and perovskite quantum dots, *Nano Energy* 50 (2018) 756–765.
- G. Liu, H. Zhao, F. Diao, Z. Ling, Y. Wang, Stable tandem luminescent solar concentrators based on CdSe/Cds quantum dots and carbon dots, *J. Mater. Chem. C* 6 (37) (2018) 10059–10066.
- J.A.H.P. Sol, V. Dehm, R. Hecht, F. Würthner, A.P.H.J. Schenning, M.G. Debije, Temperature-responsive luminescent solar concentrators: tuning energy transfer in a liquid crystalline matrix, *Angew. Chem. Int. Ed. Engl.* 57 (4) (2018) 1030–1033.
- Y. Li, P. Miao, W. Zhou, X. Gong, X. Zhao, N-doped carbon-dots for luminescent solar concentrators, *J. Mater. Chem. A* 5 (40) (2017) 21452–21459.
- J.C. de Mello, H.F. Wittmann, R.H. Friend, An improved experimental determination of external photoluminescence quantum efficiency, *Adv. Mater.* 9 (1997) 230–232.
- V.I. Klimov, T.A. Baker, J. Lim, K.A. Velizhanin, H. McDaniel, Quality factor of luminescent solar concentrators and practical concentration limits attainable with semiconductor quantum dots, *ACS Photonics* 3 (2016) 1138–1148.
- Y. Ghosh, B.D. Mangum, J.L. Casson, D.J. Williams, H. Htoon, J.A. Hollingsworth, New insights into the complexities of shell growth and the strong influence of particle volume in nonblinking “giant” core/shell nanocrystal quantum dots, *J. Am. Chem. Soc.* 134 (23) (2012) 9634–9643.
- C.J. Hanson, N.F. Hartmann, A. Singh, X. Ma, W.J.I. DeBenedetti, J.L. Casson, J.K. Grey, Y.J. Chabal, A.V. Malko, M. Sykora, A. Piryatinski, H. Htoon, J.A. Hollingsworth, Giant PbSe/CdSe/CdS quantum dots: crystal-structure-defined ultrafast near-infrared photoluminescence from single nanocrystals, *J. Am. Chem. Soc.* 139 (32) (2017) 11081–11088.
- P. Reiss, M. Protière, L. Li, Core/shell semiconductor nanocrystals, *Small* 5 (2009) 154–168.
- H. Zhao, G. Liu, F. Vidal, Y. Wang, A. Vomiero, Colloidal thick-shell pyramidal quantum dots for efficient hydrogen production, *Nano Energy* 53 (2018) 116–124.
- F. Ren, S.A. Lindley, H. Zhao, L. Tan, B.A. Gonfa, Y.C. Pu, F. Yang, X. Liu, F. Vidal, J.Z. Zhang, F. Vetrone, D. Ma, Towards understanding the unusual photoluminescence intensity variation of ultrasmall colloidal PbS quantum dots with the formation of a thin CdS shell, *Phys. Chem. Chem. Phys.* 18 (46) (2016) 31828–31835.
- J. Zhou, M. Zhu, R. Meng, H. Qin, X. Peng, Ideal CdSe/CdS core/shell nanocrystals enabled by entropic ligands and their core size-, shell thickness-, and ligand-dependent photoluminescence properties, *J. Am. Chem. Soc.* 139 (46) (2017) 16556–16567.
- H. Liu, S. Li, W. Chen, D. Wang, C. Li, D. Wu, J. Hao, Z. Zhou, X. Wang, K. Wang, Scattering enhanced quantum dots based luminescent solar concentrators by silica nanoparticles, *Sol. Energy Mater. Sol. Cell.* 179 (2018) 380–385.
- J.S. Batchelder, A.H. Zewail, T. Cole, Luminescent solar concentrators I: theory of operation and techniques for performance evaluation, *Appl. Opt.* 18 (18) (1979) 3090–3110.
- J. Roncali, F. Garnier, Photon-transport properties of luminescent solar concentrators: analysis and optimization, *Appl. Opt.* 23 (16) (1984) 2809–2817.
- S. McDowall, T. Butler, E. Bain, K. Scharnhorst, D. Patrick, Comprehensive analysis of escape-cone losses from luminescent waveguides, *Appl. Opt.* 52 (6) (2013) 1230–1239.